

Three-band tight-binding model for monolayers of group-VIB transition metal dichalcogenides

Gui-Bin Liu,^{1,2} Wen-Yu Shan,³ Yugui Yao,¹ Wang Yao,^{2,*} and Di Xiao^{3,†}

¹*School of Physics, Beijing Institute of Technology, Beijing 100081, China*

²*Department of Physics and Center of Theoretical and Computational Physics, The University of Hong Kong, Hong Kong, China*

³*Department of Physics, Carnegie Mellon University, Pittsburgh, Pennsylvania 15213, USA*

(Dated: December 3, 2024)

We present a three-band tight-binding (TB) model for describing the low-energy physics in monolayers of group-VIB transition metal dichalcogenides MX_2 ($M=\text{Mo, W}$; $X=\text{S, Se, Te}$). As the conduction and valence band edges are predominantly contributed by the d_{z^2} , d_{xy} , and $d_{x^2-y^2}$ orbitals of M atoms, the TB model is constructed using these three orbitals based on the symmetries of the monolayers. Parameters of the TB model are fitted from the first-principles energy bands for all MX_2 monolayers. The TB model involving only the nearest-neighbor M - M hoppings is sufficient to capture the band-edge properties in the $\pm K$ valleys, including the energy dispersions as well as the Berry curvatures. The TB model involving up to the third-nearest-neighbor M - M hoppings can well reproduce the energy bands in the entire Brillouin zone. Spin-orbit coupling in valence bands is well accounted for by including the on-site spin-orbit interactions of M atoms. The conduction band also exhibits a small valley-dependent spin splitting which has an overall sign difference between MoX_2 and WX_2 . We discuss the origins of these corrections to the three-band model. The three-band TB model developed here is efficient to account for low-energy physics in MX_2 monolayers, and its simplicity can be particularly useful in the study of many-body physics and physics of edge states.

PACS numbers: 71.15.-m, 73.22.-f, 73.61.Le

I. INTRODUCTION

Recently, monolayers of group-VIB transition metal dichalcogenides MX_2 ($M = \text{Mo, W}$; $X = \text{S, Se}$) have attracted significant interest due to their extraordinary electronic and optical properties. These two-dimensional semiconductors possess a direct bandgap¹⁻⁵ in the visible frequency range and exhibit excellent mobility at room temperature,⁶⁻¹¹ making them promising candidates for electronic and optoelectronic applications.¹²

MX_2 monolayers can be regarded as the semiconductor analog of graphene, with both the conduction and valence band edges located at the two corners of the first Brillouin zone (BZ), i.e. K and $-K$ points [Fig. 1(c)]. Thus, electrons and holes acquire an extra valley degree of freedom, which may be used for information encoding and processing.¹³⁻¹⁷ Following earlier theoretical studies,^{13,14} it was predicted that inversion symmetry breaking in monolayer MX_2 gives rise to valley dependent optical transition selection rule, where inter-band transitions in K and $-K$ valleys couple preferentially to left- and right-circularly polarized light.^{18,19} This prediction has led to the first experimental observations of dynamical pumping of valley polarization by circularly polarized light in monolayers of MoS_2 ,¹⁹⁻²¹ followed by the demonstration of electric control of valley circular dichroism in bilayer MoS_2 ²² and valley coherence in monolayer WSe_2 .²³ Moreover, because of the giant spin-orbit coupling (SOC) in the material,²⁴ the absence of inversion symmetry also allows a strong coupling between the spin and the valley degrees of freedom.¹⁸ These results suggest that monolayer MX_2 could possibly be the host for integrated spintronics and valleytronics.

In Ref. 18 where the valley and spin coupled physics is first predicted in monolayer MX_2 , an effective two-band $\mathbf{k} \cdot \mathbf{p}$ model is given based on symmetry considerations, which suggests that the band edge electrons and holes can be described

as massive Dirac fermions. This $\mathbf{k} \cdot \mathbf{p}$ model has also been applied to study the transport, optical, and magnetic properties of MX_2 monolayers²⁵⁻²⁷ and bilayers.^{22,28} However, the $\mathbf{k} \cdot \mathbf{p}$ model is only valid close to the band edge. To obtain a more accurate description of the band structure, several tight-binding (TB) and $\mathbf{k} \cdot \mathbf{p}$ models have been recently introduced at the expense of including more orbitals into the Hamiltonian.²⁹⁻³²

In this paper, we develop a minimal symmetry-based three-band TB model using only the M - d_{z^2} , d_{xy} , and $d_{x^2-y^2}$ orbitals. We show that, by including only the nearest-neighbor (NN) hoppings, this TB model is sufficient to capture the band-edge properties in the $\pm K$ valleys, including the energy dispersions as well as the Berry curvatures. By including up to the third-nearest-neighbor (TNN) M - M hoppings, our model can well reproduce the energy bands in the entire BZ. All parameters in our model are determined accurately by fitting the first-principles (FP) energy bands and results for $X = \text{Te}$ are also shown for systematical purpose although MTe_2 monolayers are not realized experimentally now. SOC effects are studied under the approximation of on-site spin-orbit interaction, which results in a large valence-band spin splitting at the K point. Besides, for the small but finite conduction-band spin splitting at K recently noted,³³⁻³⁷ we reveal here a sign difference between MoX_2 and WX_2 , and show that such splitting can be partly accounted for by perturbative corrections to the three-band model. Our model provides a minimal starting point to include various interaction effects.

This paper is organized as follows. In Sec. II, we introduce our three-band TB model and fitting results. In Sec. III, SOC effects are studied. Conclusions are given in Sec. IV. In addition, an application of the TB model in zigzag nanoribbon is demonstrated in Appendix A. The relation between the $\mathbf{k} \cdot \mathbf{p}$ model in Ref. 18 and this TB model is shown in Appendix B. The FP method is given in Appendix C.

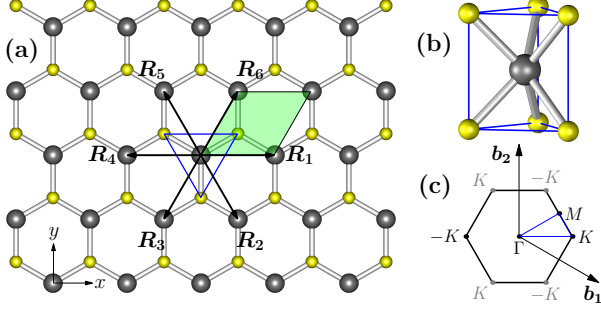


Figure 1: (color online) (a) Top view of monolayer MX_2 . Big ball is M and small ball is X . $R_1 \sim R_6$ show the M - M nearest neighbors. The shadowed diamond region shows the 2D unit cell with lattice constant a . (b) Schematic for the structure of trigonal prismatic coordination, corresponding to the blue triangle in (a). (c) The 2D first Brillouin zone with special \mathbf{k} points. b_1 and b_2 are the reciprocal basis vectors. The two inequivalent valleys K and $-K$ are shown in black and their equivalent counterparts in gray.

II. THE THREE-BAND TB MODEL

For simplicity we first introduce the spinless model and SOC will be considered in the next Section. In the following, we first analyze the symmetries and orbitals to determine the bases, then give the three-band TB model involving NN M - M hoppings, and finally introduce up to TNN hoppings to improve the TB bands.

A. Symmetries, orbitals and bases

Monolayer MX_2 has the D_{3h} point-group symmetry and its structure is shown in Fig. 1. From early theoretical studies^{38,39} and recent FP investigations^{24,34,40,41} we know that the Bloch states of monolayer MoS_2 near the band edges mostly consist of Mo d orbitals, especially the d_{z^2} , d_{xy} and $d_{x^2-y^2}$ orbitals. Figure 2 clearly shows that contributions from s orbitals are negligible, those from p orbitals are very small near the band edges, and d_{z^2} , d_{xy} and $d_{x^2-y^2}$ orbitals are dominant components for conduction and valence bands. The trigonal prismatic coordination [Fig. 1(b)] splits the Mo d orbitals into three categories:³⁹ $A'_1\{d_{z^2}\}$, $E'\{d_{xy}, d_{x^2-y^2}\}$, and $E''\{d_{xz}, d_{yz}\}$, where A'_1 , E' , and E'' are the Mulliken notations for the irreducible representations (IRs) of point group D_{3h} . The reflection symmetry by the xy plane, $\hat{\sigma}_h$, allows hybridization only between orbitals in A'_1 and E' categories, leaving E'' decoupled from A'_1 and E' bands [Fig. 2(a)]. In fact, the above analyses are also true for all monolayers of MX_2 . Therefore, it is reasonable to construct a three-band TB model of monolayer MX_2 which can capture the main low-energy physics by considering d - d hoppings using the minimal set of M - d_{z^2} , d_{xy} and $d_{x^2-y^2}$ orbitals as bases. Obviously, using only the three d orbitals and neglecting X - p orbitals for the bases is an approximation, which will be referred as the “three-band approximation” hereinafter.

To conveniently describe the atomic bases by the symmetry

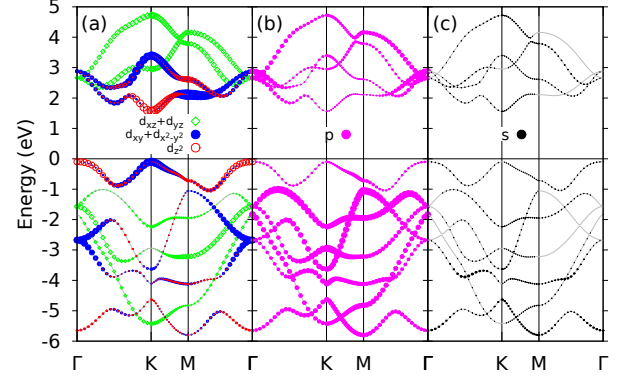


Figure 2: (color online) Orbital projected band structures for monolayer MoS_2 from FP calculations. Fermi energy is set to zero. Symbol size is proportional to its population in corresponding state. (a) Contributions from Mo d orbitals: blue dots for d_{xy} and $d_{x^2-y^2}$, red open circles for d_{z^2} , and green open diamonds for d_{xz} and d_{yz} . (b) Total p orbitals, dominated by S atoms. (c) Total s orbitals.

of D_{3h} point group, we denote them as $|\phi_\mu^j\rangle$ ($\mu = 1, \dots, l_j$) in terms of the μ -th basis belonging to the j -th IR:

$$|\phi_1^1\rangle = d_{z^2}, \quad |\phi_1^2\rangle = d_{xy}, \quad |\phi_2^2\rangle = d_{x^2-y^2}, \quad (1)$$

where $j = 1$ stands for A'_1 , $j = 2$ for E' , and l_j for the dimension of the j -th IR. Then the matrix elements of the Hamiltonian \hat{H} can be easily obtained as $H_{\mu\mu'}^{jj'}(\mathbf{k}) = \sum_{\mathbf{R}} e^{i\mathbf{k}\cdot\mathbf{R}} E_{\mu\mu'}^{jj'}(\mathbf{R})$ in which

$$E_{\mu\mu'}^{jj'}(\mathbf{R}) = \langle \phi_\mu^j(\mathbf{r}) | \hat{H} | \phi_{\mu'}^{j'}(\mathbf{r} - \mathbf{R}) \rangle \quad (2)$$

is the hopping integral between the atomic orbitals $|\phi_\mu^j\rangle$ at $\mathbf{0}$ and $|\phi_{\mu'}^{j'}\rangle$ at lattice vector \mathbf{R} . Given $E_{\mu\mu'}^{jj'}(\mathbf{R})$, the hopping integrals to all neighboring sites can be generated by

$$E_{\mu\mu'}^{jj'}(\hat{g}_n \mathbf{R}) = D^j(\hat{g}_n) E_{\mu\mu'}^{jj'}(\mathbf{R}) [D^{j'}(\hat{g}_n)]^\dagger, \quad (3)$$

where $D^j(\hat{g}_n)$ with dimension $l_j \times l_j$ is the matrix of the j -th IR and $E_{\mu\mu'}^{jj'}(\mathbf{R})$ with dimension $l_j \times l_{j'}$ is the matrix composed of $E_{\mu\mu'}^{jj'}(\mathbf{R})$. \hat{g} 's are a subset of the symmetry operations of D_{3h} , $\{\hat{E}, \hat{C}_3, \hat{C}_3^2, \hat{\sigma}_v, \hat{\sigma}_v', \hat{\sigma}_v''\}$, where \hat{E} is the identity operation, \hat{C}_3 is the rotation by $2\pi/3$ around the z axis, $\hat{\sigma}_v$ is the reflection by the plane perpendicular to the xy plane and through the angular bisector of \mathbf{R}_1 and \mathbf{R}_6 in Fig. 1(a), and $\hat{\sigma}_v'$ and $\hat{\sigma}_v''$ are obtained through rotating $\hat{\sigma}_v$ around z axis by $2\pi/3$ and $4\pi/3$ respectively. Using the above symmetry relation, we can reduce the parameters, i.e. the hopping integrals, to a minimal set. We emphasize that these symmetry-based d - d hoppings include not only the direct d - d interactions of M atoms but also the indirect interactions mediated by X - p orbitals.

B. Model with nearest-neighbor hoppings

In this subsection, we introduce the three-band TB model involving only NN d - d hoppings, which is referred to as “NN TB” in the following. After determining each Hamiltonian matrix element, we get the three-band NN TB Hamiltonian as

$$H^{\text{NN}}(\mathbf{k}) = \begin{bmatrix} h_0 & h_1 & h_2 \\ h_1^* & h_{11} & h_{12} \\ h_2^* & h_{12}^* & h_{22} \end{bmatrix}, \quad (4)$$

in which

$$h_0 = 2t_0(\cos 2\alpha + 2\cos \alpha \cos \beta) + \epsilon_1, \quad (5)$$

$$h_1 = -2\sqrt{3}t_2 \sin \alpha \sin \beta + 2it_1(\sin 2\alpha + \sin \alpha \cos \beta), \quad (6)$$

$$h_2 = 2t_2(\cos 2\alpha - \cos \alpha \cos \beta) + 2\sqrt{3}it_1 \cos \alpha \sin \beta, \quad (7)$$

$$h_{11} = 2t_{11} \cos 2\alpha + (t_{11} + 3t_{22}) \cos \alpha \cos \beta + \epsilon_2, \quad (8)$$

$$h_{22} = 2t_{22} \cos 2\alpha + (3t_{11} + t_{22}) \cos \alpha \cos \beta + \epsilon_2, \quad (9)$$

$$h_{12} = \sqrt{3}(t_{22} - t_{11}) \sin \alpha \sin \beta + 4it_{12} \sin \alpha (\cos \alpha - \cos \beta), \quad (10)$$

$$(\alpha, \beta) = \left(\frac{1}{2}k_x a, \frac{\sqrt{3}}{2}k_y a \right), \quad (11)$$

$$\begin{aligned} t_0 &= E_{11}^{11}(\mathbf{R}_1), & t_1 &= E_{11}^{12}(\mathbf{R}_1), & t_2 &= E_{12}^{12}(\mathbf{R}_1), \\ t_{11} &= E_{11}^{22}(\mathbf{R}_1), & t_{12} &= E_{12}^{22}(\mathbf{R}_1), & t_{22} &= E_{22}^{22}(\mathbf{R}_1), \end{aligned} \quad (12)$$

and ϵ_j is the on-site energy corresponding to the atomic orbital $|\phi_\mu^j\rangle$. Note that, for simplicity, we have assumed the orthogonality between each pair of different bases, therefore the overlapping matrix of the bases is omitted and only the Hamiltonian matrix $H^{\text{NN}}(\mathbf{k})$ is considered. Confined by the symmetry of the system, there are eight independent parameters in $H^{\text{NN}}(\mathbf{k})$: $\epsilon_1, \epsilon_2, t_0, t_1, t_2, t_{11}, t_{12}$, and t_{22} .

In order to determine the eight parameters in the TB model accurately, we fit the band structures according to the FP results. There is no definitive strategy to fit the bands. In our case, since we are mostly interested in the low-energy physics near the $\pm K$ points and our analysis is entirely symmetry based, we will fit the band energies at the high-symmetry \mathbf{k} points, namely Γ , K , and M (listed in Table I), together with least squares fitting according to the energies of the conduction and valence bands near K .

By fitting the FP band structures of relaxed monolayers of MX_2 in both generalized-gradient approximation (GGA) and

Table I: Band energies at the high-symmetry \mathbf{k} points analytically obtained from the TB Hamiltonian Eq. (4). The energies at each \mathbf{k} point are in ascending order. $t_{12} > 0$ is assumed.

$\Gamma = (0, 0)$	$K = (\frac{4\pi}{3a}, 0)$	$M = (\frac{\pi}{a}, \frac{\pi}{\sqrt{3}a})$
$\epsilon_1 + 6t_0$	$\epsilon_2 - \frac{3}{2}(t_{11} + t_{22}) - 3\sqrt{3}t_{12}$	$f_1 - f_2^a$
$\epsilon_2 + 3(t_{11} + t_{22})$	$\epsilon_1 - 3t_0$	$\epsilon_2 + t_{11} - 3t_{22}$
	$\epsilon_2 - \frac{3}{2}(t_{11} + t_{22}) + 3\sqrt{3}t_{12}$	$f_1 + f_2$
^a f_1 and f_2 are functions independent of t_1 : $f_1 = \frac{1}{2}(\epsilon_1 + \epsilon_2) - t_0 - \frac{3}{2}t_{11} + \frac{1}{2}t_{22}$, $f_2 = \frac{1}{2}\sqrt{(\epsilon_1 - \epsilon_2 - 2t_0 + 3t_{11} - t_{22})^2 + 64t_{12}^2}$.		

local-density approximation (LDA) cases, we get the TB parameters listed in Table II and the corresponding band structures shown in Fig. 3. The FP results (lattice parameters and band structures) obtained here are consistent with previous works.^{24,41–45} In Fig. 3, by comparing the TB bands with the FP bands from d_{z^2} , d_{xy} , and $d_{x^2-y^2}$ orbitals, we can see that the former agree well with the latter near the conduction-band minimum (CBM) and valence-band maximum (VBM) at K for all the MX_2 monolayers, but significantly deviate from the latter in other regions. This is because the three-band approximation neglects the p orbitals of X atoms which still have substantial contributions to the conduction bands at Γ and valence bands at M [Fig. 2(b)]. Nevertheless, this simple NN TB model is sufficient to describe the physics of conduction and valence bands in $\pm K$ valleys. In addition, a trial model Hamiltonian of MX_2 zigzag nanoribbon based on this simple NN TB model can give reasonable edge states (see Appendix A).

We note that the band structure is very sensitive to the lattice constant:^{46–50} in Fig. 3(a) the valence-band energy at Γ is higher than at K by 4meV, and in Fig. 3(i) and 3(j) the conduction-band energy at the dip near the midway of Γ and K is lower than at K by 5meV and 59meV respectively. This contradicts with the observed direct bandgaps. This is related to the different relaxed lattice constants between GGA and LDA (GGA tends to overestimate the lattice constant whereas LDA underestimate it, see Table II). This, however, has little effect on our fitting at the K point.

C. Model with up to third-nearest-neighbor hoppings

In order to reproduce the energy bands in the entire BZ, we further consider up to the TNN M - M hoppings. By the same symmetry-based procedure, we derive the three-band TNN model Hamiltonian $H^{\text{TNN}}(\mathbf{k})$ as

$$H^{\text{TNN}}(\mathbf{k}) = \begin{bmatrix} V_0 & V_1 & V_2 \\ V_1^* & V_{11} & V_{12} \\ V_2^* & V_{12}^* & V_{22} \end{bmatrix}, \quad (13)$$

Table II: Fitted parameters of the three-band NN TB model based on the FP band structures of monolayer MX_2 using both GGA and LDA. a and z_{X-X} are the relaxed lattice constant and $X-X$ distance in z direction respectively. The energy parameters $\epsilon_1 \sim t_{22}$ are in unit eV.

	a (Å)	z_{X-X} (Å)	ϵ_1	ϵ_2	t_0	t_1	t_2	t_{11}	t_{12}	t_{22}
GGA										
MoS ₂	3.190	3.130	1.046	2.104	-0.184	0.401	0.507	0.218	0.338	0.057
WS ₂	3.191	3.144	1.130	2.275	-0.206	0.567	0.536	0.286	0.384	-0.061
MoSe ₂	3.326	3.345	0.919	2.065	-0.188	0.317	0.456	0.211	0.290	0.130
WSe ₂	3.325	3.363	0.943	2.179	-0.207	0.457	0.486	0.263	0.329	0.034
MoTe ₂	3.557	3.620	0.605	1.972	-0.169	0.228	0.390	0.207	0.239	0.252
WTe ₂	3.560	3.632	0.606	2.102	-0.175	0.342	0.410	0.233	0.270	0.190
LDA										
MoS ₂	3.129	3.115	1.238	2.366	-0.218	0.444	0.533	0.250	0.360	0.047
WS ₂	3.132	3.126	1.355	2.569	-0.238	0.626	0.557	0.324	0.405	-0.076
MoSe ₂	3.254	3.322	1.001	2.239	-0.222	0.350	0.488	0.244	0.314	0.129
WSe ₂	3.253	3.338	1.124	2.447	-0.242	0.506	0.514	0.305	0.353	0.025
MoTe ₂	3.472	3.598	0.618	2.126	-0.202	0.254	0.423	0.241	0.263	0.269
WTe ₂	3.476	3.611	0.623	2.251	-0.209	0.388	0.442	0.272	0.295	0.200

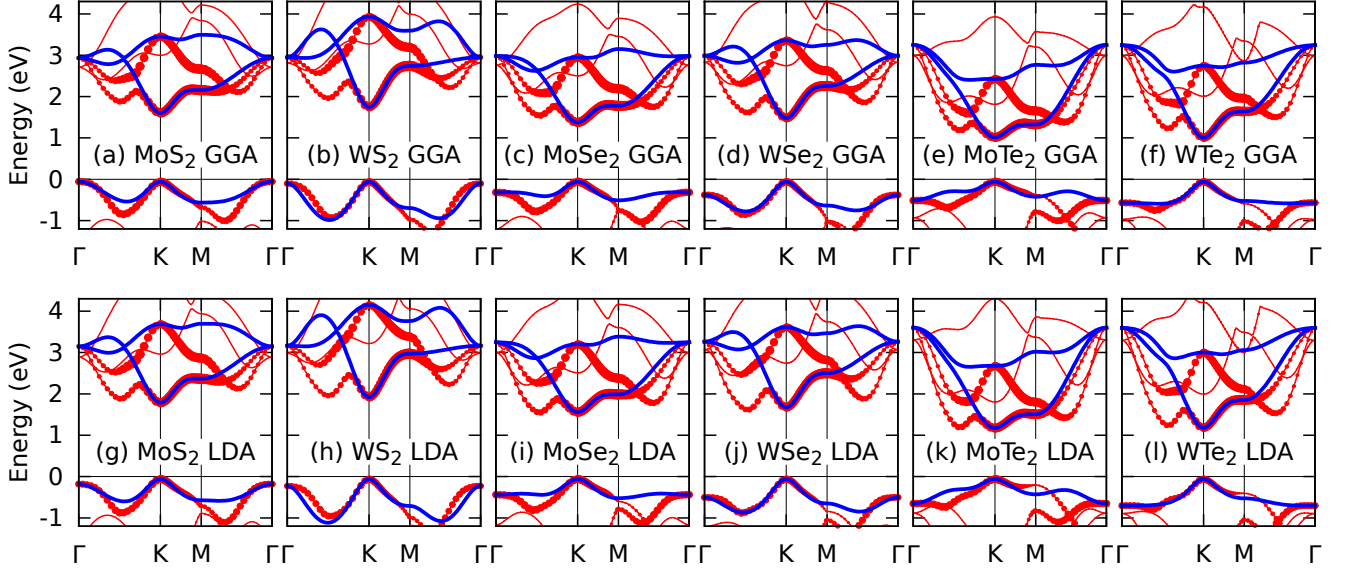


Figure 3: (color online) The NN TB band structures (blue or dark curves) of MX_2 monolayers compared with the FP ones (red or gray curves and dots). VBMs are shifted to zero. The dots show the band components from d_{z^2} , d_{xy} , and $d_{x^2-y^2}$ orbitals, with which the TB bands should compare. (a)~(f) for GGA and (g)~(l) for LDA.

in which

$$\begin{aligned}
 V_0 = & \epsilon_1 + 2t_0(2\cos\alpha\cos\beta + \cos 2\alpha) \\
 & + 2r_0(2\cos 3\alpha\cos\beta + \cos 2\beta) \\
 & + 2u_0(2\cos 2\alpha\cos 2\beta + \cos 4\alpha), \quad (14)
 \end{aligned}$$

$$\begin{aligned}
 \text{Re}[V_1] = & -2\sqrt{3}t_2\sin\alpha\sin\beta \\
 & + 2(r_1 + r_2)\sin 3\alpha\sin\beta \\
 & - 2\sqrt{3}u_2\sin 2\alpha\sin 2\beta, \quad (15)
 \end{aligned}$$

$$\begin{aligned}
 \text{Im}[V_1] = & 2t_1\sin\alpha(2\cos\alpha + \cos\beta) \\
 & + 2(r_1 - r_2)\sin 3\alpha\cos\beta \\
 & + 2u_1\sin 2\alpha(2\cos 2\alpha + \cos 2\beta), \quad (16)
 \end{aligned}$$

$$\begin{aligned}
 \text{Re}[V_2] = & +2t_2(\cos 2\alpha - \cos\alpha\cos\beta) \\
 & - \frac{2}{\sqrt{3}}(r_1 + r_2)(\cos 3\alpha\cos\beta - \cos 2\beta) \\
 & + 2u_2(\cos 4\alpha - \cos 2\alpha\cos 2\beta), \quad (17)
 \end{aligned}$$

Table III: Fitted parameters (unit: eV) for the three-band TNN TB model based on the FP bands in both GGA and LDA cases.

	ϵ_1	ϵ_2	t_0	t_1	t_2	t_{11}	t_{12}	t_{22}	r_0	r_1
	r_2	r_{11}	r_{12}	u_0	u_1	u_2	u_{11}	u_{12}	u_{22}	
GGA										
MoS ₂	0.683	1.707	-0.146	-0.114	0.506	0.085	0.162	0.073	0.060	-0.236
	0.067	0.016	0.087	-0.038	0.046	0.001	0.266	-0.176	-0.150	
WS ₂	0.717	1.916	-0.152	-0.097	0.590	0.047	0.178	0.016	0.069	-0.261
	0.107	-0.003	0.109	-0.054	0.045	0.002	0.325	-0.206	-0.163	
MoSe ₂	0.684	1.546	-0.146	-0.130	0.432	0.144	0.117	0.075	0.039	-0.209
	0.069	0.052	0.060	-0.042	0.036	0.008	0.272	-0.172	-0.150	
WSe ₂	0.728	1.655	-0.146	-0.124	0.507	0.117	0.127	0.015	0.036	-0.234
	0.107	0.044	0.075	-0.061	0.032	0.007	0.329	-0.202	-0.164	
MoTe ₂	0.588	1.303	-0.226	-0.234	0.036	0.400	0.098	0.017	0.003	-0.025
	-0.169	0.082	0.051	0.057	0.103	0.187	-0.045	-0.141	0.087	
WTe ₂	0.697	1.380	-0.109	-0.164	0.368	0.204	0.093	0.038	-0.015	-0.209
	0.107	0.115	0.009	-0.066	0.011	-0.013	0.312	-0.177	-0.132	
LDA										
MoS ₂	0.820	1.931	-0.176	-0.101	0.531	0.084	0.169	0.070	0.070	-0.252
	0.084	0.019	0.093	-0.043	0.047	0.005	0.304	-0.192	-0.162	
WS ₂	0.905	2.167	-0.175	-0.090	0.611	0.043	0.181	0.008	0.075	-0.282
	0.127	0.001	0.114	-0.063	0.047	0.004	0.374	-0.224	-0.177	
MoSe ₂	0.715	1.687	-0.154	-0.134	0.437	0.124	0.119	0.072	0.048	-0.248
	0.090	0.066	0.045	-0.067	0.041	0.005	0.327	-0.194	-0.151	
WSe ₂	0.860	1.892	-0.152	-0.125	0.508	0.094	0.129	0.009	0.044	-0.278
	0.129	0.059	0.058	-0.090	0.039	0.001	0.392	-0.224	-0.165	
MoTe ₂	0.574	1.410	-0.148	-0.173	0.333	0.203	0.186	0.127	0.007	-0.280
	0.067	0.073	0.081	-0.054	0.008	0.037	0.145	-0.078	0.035	
WTe ₂	0.675	1.489	-0.124	-0.159	0.362	0.196	0.101	0.044	-0.009	-0.250
	0.129	0.131	-0.007	-0.086	0.012	-0.020	0.361	-0.193	-0.129	

$$\begin{aligned} \text{Im}[V_2] &= 2\sqrt{3}t_1 \cos \alpha \sin \beta \\ &+ \frac{2}{\sqrt{3}} \sin \beta (r_1 - r_2) (\cos 3\alpha + 2 \cos \beta) \\ &+ 2\sqrt{3}u_1 \cos 2\alpha \sin 2\beta, \quad (18) \end{aligned}$$

$$\begin{aligned} V_{11} &= \epsilon_2 + (t_{11} + 3t_{22}) \cos \alpha \cos \beta + 2t_{11} \cos 2\alpha \\ &+ 4r_{11} \cos 3\alpha \cos \beta + 2(r_{11} + \sqrt{3}r_{12}) \cos 2\beta \\ &+ (u_{11} + 3u_{22}) \cos 2\alpha \cos 2\beta + 2u_{11} \cos 4\alpha, \quad (19) \end{aligned}$$

$$\begin{aligned} \text{Re}[V_{12}] &= \sqrt{3}(t_{22} - t_{11}) \sin \alpha \sin \beta + 4r_{12} \sin 3\alpha \sin \beta \\ &+ \sqrt{3}(u_{22} - u_{11}) \sin 2\alpha \sin 2\beta, \quad (20) \end{aligned}$$

$$\begin{aligned} \text{Im}[V_{12}] &= 4t_{12} \sin \alpha (\cos \alpha - \cos \beta) \\ &+ 4u_{12} \sin 2\alpha (\cos 2\alpha - \cos 2\beta), \quad (21) \end{aligned}$$

and

$$\begin{aligned} V_{22} &= \epsilon_2 + (3t_{11} + t_{22}) \cos \alpha \cos \beta + 2t_{22} \cos 2\alpha \\ &+ 2r_{11} (2 \cos 3\alpha \cos \beta + \cos 2\beta) \\ &+ \frac{2}{\sqrt{3}} r_{12} (4 \cos 3\alpha \cos \beta - \cos 2\beta) \\ &+ (3u_{11} + u_{22}) \cos 2\alpha \cos 2\beta + 2u_{22} \cos 4\alpha. \quad (22) \end{aligned}$$

The additional parameters are defined as

$$\begin{aligned} r_0 &= E_{11}^{11}(\tilde{\mathbf{R}}_1), \quad r_1 = E_{11}^{12}(\tilde{\mathbf{R}}_1), \quad r_2 = E_{12}^{12}(\tilde{\mathbf{R}}_1), \\ r_{11} &= E_{11}^{22}(\tilde{\mathbf{R}}_1), \quad r_{12} = E_{12}^{22}(\tilde{\mathbf{R}}_1) \end{aligned} \quad (23)$$

and

$$\begin{aligned} u_0 &= E_{11}^{11}(2\mathbf{R}_1), \quad u_1 = E_{11}^{12}(2\mathbf{R}_1), \quad u_2 = E_{12}^{12}(2\mathbf{R}_1), \\ u_{11} &= E_{11}^{22}(2\mathbf{R}_1), \quad u_{12} = E_{12}^{22}(2\mathbf{R}_1), \quad u_{22} = E_{22}^{22}(2\mathbf{R}_1), \end{aligned} \quad (24)$$

in which $\tilde{\mathbf{R}}_1 = \mathbf{R}_1 + \mathbf{R}_2$ is one of the next-NN vectors and $2\mathbf{R}_1$ is one of the TNN vectors.The fitted parameters for $H^{\text{TNN}}(\mathbf{k})$ are listed in Table III and the corresponding bands are shown in Fig. 4 from which

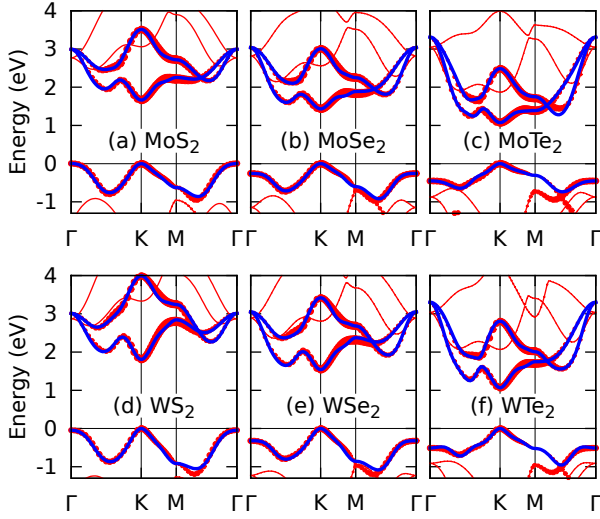


Figure 4: (color online) Energy bands from the TNN TB model (blue or dark curves) of MX_2 monolayers compared with the FP ones in GGA case (red or gray curves and dots). The dots show the band components from d_{z^2} , d_{xy} , and $d_{x^2-y^2}$ orbitals, with which the TB bands should compare.

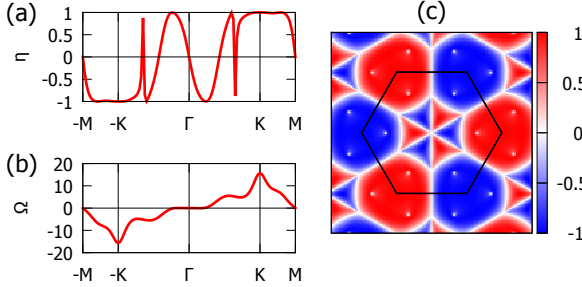


Figure 5: (color online) Quantities from the TNN TB for monolayer MoS_2 under GGA parameters: (a) Degree of circular polarization, $\eta(\mathbf{k})$, and (b) Berry curvature $\Omega(\mathbf{k})$ in unit \AA^2 along \mathbf{k} -path $-M \rightarrow -K \rightarrow \Gamma \rightarrow K \rightarrow M$. (c) Color map of $\eta(\mathbf{k})$ where the hexagon shows the BZ.

we can see that the three TB bands agree well with the FP ones contributed by d_{z^2} , d_{xy} and $d_{x^2-y^2}$ orbitals in the entire BZ. The well reproduced bands mean that effective masses can be obtained accurately by this TNN TB model. In addition, we show the Berry curvatures calculated using this TB model in Fig. 5(b) which shows good agreement with the result in Ref. 51. We note that around the Γ point, the conduction bands with the lowest energies are made of d_{xz} , d_{yz} and X - p orbitals, which cannot be captured by our three-band model.

It should be noted that energy bands are only one aspect of physical properties and hence not enough to capture all physics. We also calculated the \mathbf{k} -resolved degree of circular polarization for absorbed photons, $\eta(\mathbf{k})$. As shown in Ref. 19, $\eta(\mathbf{k})$ has the same sign in each region of $1/6$ of the BZ around each K or $-K$ points and exhibits high degree of polarization in most of each region. We can see that the $\eta(\mathbf{k})$ calculated using the TB model here can give correct values

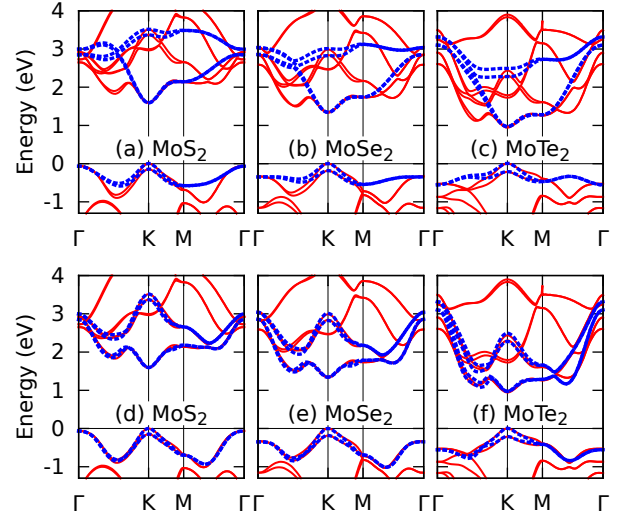


Figure 6: (color online) Energy bands of monolayers MoX_2 with SOC. Thick blue dashed curves are the TB bands: (a)~(c) from the NN TB model and (d)~(f) from the TNN TB model. Thin red solid curves are FP results with GGA. VBMs are shifted to zero.

in the large neighborhood of $\pm K$, but not in the small region around Γ [see Fig. 5(a) and (c)] due to the limitation of the three-band approximation. It can be seen from Fig. 3 and Fig. 5 that the three-band approximation works well around the $\pm K$ valleys and also the valence-band Γ point, where d orbitals dominate, but not in the k -space region where X - p orbitals are important.

III. SPIN-ORBIT COUPLING

A. The model with SOC

Due to the heavy transition-metal M atom, its SOC can be large. The large SOC of monolayer MX_2 is a fascinating feature which leads to its rich physics. For simplicity, here we approximate the SOC by considering only the on-site contribution, namely, the $\mathbf{L} \cdot \mathbf{S}$ term from M atoms. Using the bases $\{|d_{z^2}, \uparrow\rangle, |d_{xy}, \uparrow\rangle, |d_{x^2-y^2}, \uparrow\rangle, |d_{z^2}, \downarrow\rangle, |d_{xy}, \downarrow\rangle, |d_{x^2-y^2}, \downarrow\rangle\}$, we get the SOC contribution to the Hamiltonian as

$$H' = \lambda \mathbf{L} \cdot \mathbf{S} = \frac{\lambda}{2} \begin{bmatrix} L_z & 0 \\ 0 & -L_z \end{bmatrix}, \quad (25)$$

in which

$$L_z = \begin{bmatrix} 0 & 0 & 0 \\ 0 & 0 & 2i \\ 0 & -2i & 0 \end{bmatrix} \quad (26)$$

is the matrix of \hat{L}_z (z component of the orbital angular momentum) in bases of d_{z^2} , d_{xy} , and $d_{x^2-y^2}$, and λ characterizes the strength of SOC. Note that, under the three bases, the matrix elements of \hat{L}_x and \hat{L}_y are all zeroes. Then we get the full

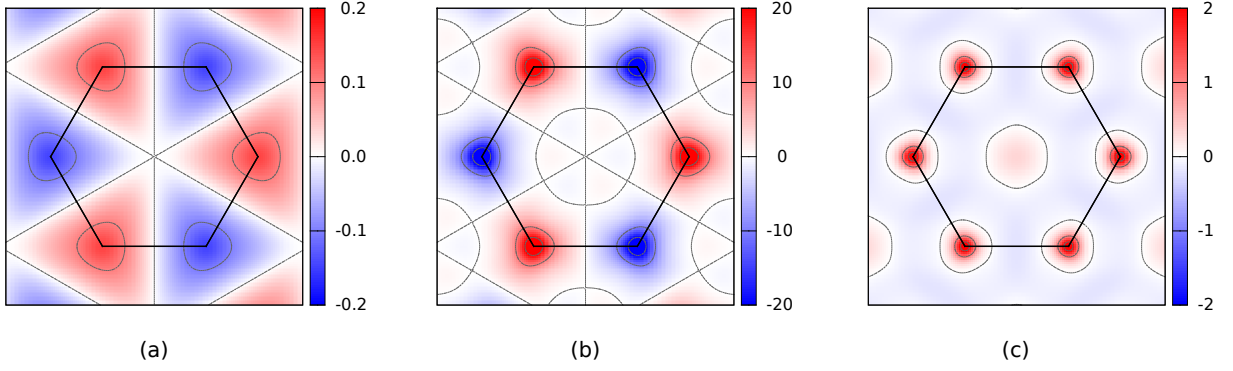


Figure 7: (color online) Contour maps in the \mathbf{k} space for monolayer MoS_2 from the NN TB model (using the GGA parameters): (a) the valence band SOC splittings in unit eV, (b) the Berry curvatures and (c) the spin Berry curvatures in unit \AA^2 . The hexagons show the BZ. The gray thin curves are the contour lines corresponding to their tick values on the color bars.

TB Hamiltonian with SOC as following

$$H_{\text{SOC}}(\mathbf{k}) = I_2 \otimes H_0(\mathbf{k}) + H' = \begin{bmatrix} H_0(\mathbf{k}) + \frac{\lambda}{2}L_z & 0 \\ 0 & H_0(\mathbf{k}) - \frac{\lambda}{2}L_z \end{bmatrix}, \quad (27)$$

in which I_2 is the 2×2 identity matrix and $H_0 = H^{\text{NN}}$ or H^{TNN} . The above Hamiltonian is block diagonal, which means that the spin z -component is not mixed by the SOC and hence is still a good quantum number due to the $\hat{\sigma}_h$ symmetry. From Eq. (27) we can easily know that at K point the SOC interaction splits VBM by $\Delta_{\text{SOC}}^{\text{v}} = 2\lambda$ and leaves CBM still degenerate (see detailed discussions in Subsection III B). The valence-band SOC (or spin) splittings are listed in the first column of Table IV. The bands from both the NN and TNN TB Hamiltonians with SOC are shown in Fig. 6 for MoX_2 . It can be seen that the NN TB bands agree well with the FP ones only for the conduction and valence bands near the K point, while the TNN TB bands agree well in the entire BZ.

Although the NN TB model is not as accurate as the TNN one, it can still give reasonable results for low-energy physics. Taking monolayer MoS_2 for example to test the NN TB model with SOC, we calculated the valence band SOC splittings and the Berry curvatures and the spin Berry curvatures, shown in Fig. 7. The valley contrasting SOC splittings $E_{\text{v}\uparrow}(\mathbf{k}) - E_{\text{v}\downarrow}(\mathbf{k})$ between the two spin split-off valence bands are clearly shown in Fig. 7(a), which agrees well with the result in Ref. 24. The Berry curvatures^{52,53} and spin Berry curvatures⁵⁴ are all peaked at $\pm K$ points, and the former have opposite signs between K and $-K$ [Fig. 7(b)] while the latter have the same signs between K and $-K$ [Fig. 7(c)]. These lead to valley Hall effect and spin Hall effect when an in-plane electric field exists.¹⁸ The TB results shown in Fig. 7(b) and (c) agree quite well with the FP results in Ref. 51. Therefore, the NN TB model is sufficient to describe correctly the physics in $\pm K$ valleys.

Table IV: The SOC splitting of valence band at K $\Delta_{\text{SOC}}^{\text{v}}$, the second-order corrected SOC parameter λ , the SOC splitting of conduction band at K from the second-order perturbation theory $\Delta_{\text{SOC}}^{\text{c(pt)}}$ and from FP bands $\Delta_{\text{SOC}}^{\text{c(FP)}}$ (GGA case), and the energy parameters in Eqs. (30) and (31). $E_{1,2} = E_{+1} - E_{+2}$, $E_{-1,0} = E_{-1} - E_0$, and $E_{1,0} = E_{+1} - E_0$. All quantities are in unit eV.

	$\Delta_{\text{SOC}}^{\text{v}}$	λ	$\Delta_{\text{SOC}}^{\text{c(pt)}}$	$\Delta_{\text{SOC}}^{\text{c(FP)}}$	$E_{1,2}$	$E_{-1,0}$	$E_{1,0}$
MoS_2	0.148	0.073	0.003	-0.003	4.840	1.395	3.176
WS_2	0.430	0.211	0.026	0.029	5.473	1.526	3.667
MoSe_2	0.184	0.091	0.007	-0.021	4.296	1.128	2.862
WSe_2	0.466	0.228	0.038	0.036	4.815	1.267	3.275
MoTe_2	0.215	0.107	0.015	-0.034	3.991	0.798	2.918
WTe_2	0.486	0.237	0.059	0.051	4.412	1.004	3.347

B. The SOC splitting of conduction band

To first-order of the SOC strength, the TB model for monolayer MX_2 here can only reproduce the large spin splitting of the valence band at K , i.e. $\Delta_{\text{SOC}}^{\text{v}}$, but gives no spin splitting of the conduction band at K , denoted by $\Delta_{\text{SOC}}^{\text{c}}$. In fact, the conduction-band spin splitting (CBSS) is not zero but a finite small value,³³⁻³⁷ and has been analyzed for MoS_2 by previous works.^{31,55} Similar to the strong valley-spin coupling in the valence band,¹⁸ the CBSS is also valley dependent due to the time-reversal symmetry and leads to weak valley-spin coupling. Through a careful examination of the FP results, we note here, for the first time, that the CBSSs of MoX_2 have opposite signs to those of WX_2 , if $\Delta_{\text{SOC}}^{\text{c}}$ is defined as the energy difference $E_{\text{c}\uparrow} - E_{\text{c}\downarrow}$ at K point (see Table IV and Fig. 8). By analyzing the FP data, we know that CBSS is induced by small contributions from M - d_{xz} , d_{yz} and X - p_x , p_y orbitals. Here we will go beyond the three-band approximation and show that a second-order perturbation correction involving M - d_{xz} and d_{yz} orbitals can partly explain the CBSSs.

FP wavefunctions show that, at K point, the Bloch waves, one below and four above the bandgap, are dominantly composed of d_{+2} , d_0 , d_{-1} , d_{-2} , and d_{+1} orbitals in ascending

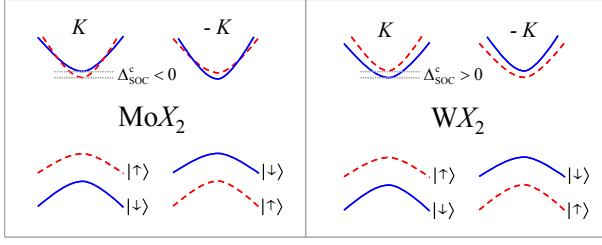


Figure 8: (color online) Schematic for the conduction and valence bands spin splittings in the $\pm K$ valleys for MoX_2 (left panel) and WX_2 (right panel). Red dashed curves are spin-up states and blue solid ones spin-down states. The conduction band spin splitting has an overall sign change between MoX_2 and WX_2 . Crossings exist for the spin-split conduction bands of MoX_2 .

order of energies respectively in the case without SOC,⁵⁶ in which $d_{\pm 2} = \frac{1}{\sqrt{2}}(d_{x^2-y^2} \pm id_{xy})$, $d_0 = d_{z^2}$, and $d_{\pm 1} = \frac{1}{\sqrt{2}}(d_{xz} \pm id_{yz})$. Accordingly, we assume that the five Bloch states are completely composed of the aforementioned five d orbitals respectively, which is a good approximation shown by the following results. To incorporate the contributions to CBSS from $d_{\pm 1}$ (i.e. d_{xz} and d_{yz}) orbitals, we make a second-order perturbation for the SOC interaction $H' = \lambda \mathbf{L} \cdot \mathbf{S}$ through the Löwdin partitioning equation:^{57,58}

$$H_{mm'}^{(2)} = \frac{1}{2} \sum_l H'_{ml} H'_{lm'} \left[\frac{1}{E_m - E_l} + \frac{1}{E_{m'} - E_l} \right], \quad (28)$$

in which $H'_{ml} = \langle d_m | H' | d_l \rangle$ ($m = \pm 2, 0$ and $l = \pm 1$) and E_m is the band energy at K corresponding to d_m orbital. Thus, the contributions from $d_{\pm 1}$ orbitals are folded into an effective second-order SOC interaction in bases $\{|d_{+2}, d_0, d_{-2}\} \otimes \{|\uparrow\rangle, |\downarrow\rangle\}$ as following

$$H'^{(2)} = \text{diag}\{0, \frac{-\lambda^2}{E_{+1} - E_{+2}}, \frac{-3\lambda^2}{2(E_{+1} - E_0)}, \frac{-3\lambda^2}{2(E_{-1} - E_0)}, \frac{\lambda^2}{E_{-2} - E_{-1}}, 0\}. \quad (29)$$

Considering the first-order SOC interaction under the same bases, $H'^{(1)} = \text{diag}\{\lambda, -\lambda, 0, 0, -\lambda, \lambda\}$, finally we get the second-order corrected splittings

$$\Delta_{\text{SOC}}^v = 2\lambda + \frac{\lambda^2}{E_{+1} - E_{+2}}, \quad (30)$$

$$\Delta_{\text{SOC}}^c = \frac{3}{2}\lambda^2 \left[\frac{1}{(E_{-1} - E_0)} - \frac{1}{(E_{+1} - E_0)} \right]. \quad (31)$$

We first get the second-order corrected λ by solving Eq. (30) and then put it into Eq. (31) to get Δ_{SOC}^c . The obtained CBSSs from perturbation $\Delta_{\text{SOC}}^{c(\text{pt})}$ are listed in Table IV and compared with the FP results $\Delta_{\text{SOC}}^{c(\text{FP})}$. The signed CBSS avoids the spurious coincidence $\Delta_{\text{SOC}}^{c(\text{pt})} = |\Delta_{\text{SOC}}^{c(\text{FP})}| = 3\text{meV}$ for MoS_2

(see Table IV). We can see that the CBSSs determined by Eq. (31) agree very well with the FP splittings for WX_2 , but not for MoX_2 . We attribute these to the competition of the two origins of CBSS: (i) the second-order perturbation due to the coupling to the remote d_{xz} and d_{yz} orbitals; (ii) the first-order effect from the small component of X - p_x and p_y orbitals. Eq. (31) contains only the origin (i) but not (ii). W atom is heavier than Mo atom, therefore the W- d orbitals are the dominant contribution of the CBSSs over X - p orbitals and thus Eq. (31) works well for WX_2 . While for MoX_2 , X - p orbitals become non-negligible for CBSSs relative to Mo- d orbitals and Eq. (31) breaks down for MoX_2 . More rigorous treatments involving X - p orbitals are needed for correctly describing the CBSSs of MoX_2 , which is out of the scope of this paper.

We also note that band crossings exist for the spin-split conduction bands of MoX_2 , but not for WX_2 , as demonstrated in Fig. 8. The distance between the crossing and K point increases from MoS_2 ($\sim 0.05 \ 2\pi/a$) to MoSe_2 ($\sim 0.15 \ 2\pi/a$), and to MoTe_2 ($\sim 0.22 \ 2\pi/a$). The band crossing arises from the spin dependence in the effective mass. At the K point of MX_2 , the spin-down carrier has larger bandgap and thus heavier effective mass (flatter band) than the spin-up one.¹⁸ Combining the different sign of CBSS, the bands shift differently for MoX_2 and WX_2 resulting the crossings in MoX_2 but not in WX_2 . In addition, for different MoX_2 , larger CBSS leads to larger distance of the crossing from the K points. Because of the trigonal warping, the distances along K - Γ and K - M directions has small difference, which is not shown in Fig. 8, and crossing appears in the K - M but not K - Γ direction for MoTe_2 due to its relatively large CBSS.

IV. CONCLUSIONS

In this paper, we have developed a minimal symmetry-based three-band TB model for monolayers of MX_2 using only the M - d_{z^2} , d_{xy} , and $d_{x^2-y^2}$ orbitals. When only NN M - M hoppings are included, this TB model is sufficient to capture the band-edge properties in the $\pm K$ valleys, including the energy dispersions as well as the Berry curvatures. By including up to the TNN M - M hoppings, the model can well reproduce the energy bands in the entire BZ. In spite of the simple NN TB model, it can describe reasonably the edge states of zigzag MX_2 ribbon that consist of d_{z^2} , d_{xy} , and $d_{x^2-y^2}$ orbitals. SOC is introduced through the approximation of on-site $\mathbf{L} \cdot \mathbf{S}$ interactions in the heavy M atoms, which lead to the giant SOC splittings of the valence bands at K . In addition, we analyzed the relatively small CBSSs at K through a second-order perturbation involving d_{xz} and d_{yz} orbitals, which works quite well for WX_2 but not for MoX_2 . This is attributed to the X - p orbitals not presented in our model. We also pointed out that the signed CBSSs have different signs between WX_2 and MoX_2 . The three-band TB model developed here is efficient to account for low-energy physics in MX_2 monolayers, and its simplicity can be particularly useful in the study of many-body physics and physics of edge states.

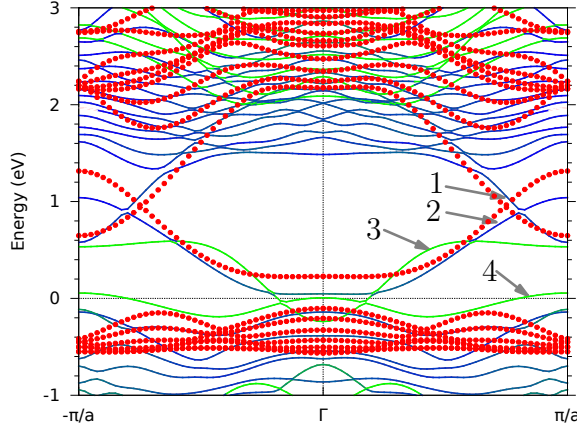


Figure 9: (color online) The energy bands for zigzag MoS₂ nanoribbon with width $W = 8$. Red dots are bands from the TB model using the GGA parameters. Curves are the FP bands, in which blue color shows the contributions from the d_{z^2} , d_{xy} , and $d_{x^2-y^2}$ orbitals and green color for other orbitals. For the bands labeled by 1 ~ 4, see the text.

Acknowledgments

The work was supported by the HKSAR Research Grant Council with Grant No. HKU706412P and the Croucher Foundation under the Croucher Innovation Award (G.B.L. and W.Y.); the National Basic Research Program of China 973 Program with Grant No. 2013CB934500 and the Basic Research Funds of Beijing Institute of Technology with Grant No. 20121842003 (G.B.L.); the National Basic Research Program of China 973 Program with Grant No. 2011CBA00100, National Natural Science Foundation of China with Grant No. 11225418 and 11174337, and Specialized Research Fund for the Doctoral Program of Higher Education of China with Grant No. 20121101110046 (Y.Y.); and the U.S. Department

of Energy, Office of Basic Energy Sciences, Materials Sciences and Engineering Division (W.S. and D.X.).

Appendix A: Model for zigzag nanoribbon

In this Appendix, we apply the three-band NN TB model to study MX_2 nanoribbons. Taking a zigzag nanoribbon in x direction with width W for example, there are W formula units in the y direction, namely $MX_2 \times W$, within an x -direction unit translational cell. The matrix elements of Hamiltonian have three types

$$H_{n\gamma, n\gamma'}^{\text{ribbon}} = \delta_{\gamma\gamma'} e_\gamma + e^{i\mathbf{k} \cdot \mathbf{R}_1} E_{\gamma\gamma'}(\mathbf{R}_1) + e^{i\mathbf{k} \cdot \mathbf{R}_4} E_{\gamma\gamma'}(\mathbf{R}_4), \quad (n = 1, \dots, W); \quad (\text{A1})$$

$$H_{n\gamma, (n-1)\gamma'}^{\text{ribbon}} = e^{i\mathbf{k} \cdot \mathbf{R}_2} E_{\gamma\gamma'}(\mathbf{R}_2) + e^{i\mathbf{k} \cdot \mathbf{R}_3} E_{\gamma\gamma'}(\mathbf{R}_3), \quad (n = 2, \dots, W); \quad (\text{A2})$$

$$H_{n\gamma, (n+1)\gamma'}^{\text{ribbon}} = e^{i\mathbf{k} \cdot \mathbf{R}_5} E_{\gamma\gamma'}(\mathbf{R}_5) + e^{i\mathbf{k} \cdot \mathbf{R}_6} E_{\gamma\gamma'}(\mathbf{R}_6), \quad (n = 1, \dots, W-1); \quad (\text{A3})$$

in which $\gamma, \gamma' \in \{1, 2, 2'\}$, $e_1^1 = \epsilon_1$, and $e_1^2 = e_2^2 = \epsilon_2$. Then we can obtain the $3W \times 3W$ Hamiltonian matrix for the zigzag nanoribbon as following

$$H^{\text{ribbon}}(k_x) = \begin{bmatrix} h'_1 & h'_2 & h'_2{}^\dagger & & \\ h'_2 & h'_1 & h'_2{}^\dagger & & \\ & h'_2 & h'_1 & \ddots & \\ & & \ddots & \ddots & h'_2{}^\dagger \\ & & & h'_2 & h'_1 \end{bmatrix}, \quad (\text{A4})$$

in which $h'_1 \equiv H_{nn}^{\text{ribbon}}$, $h'_2 \equiv H_{n, n-1}^{\text{ribbon}}$ and

$$h'_1 = \begin{bmatrix} \epsilon_1 + 2 \cos(k_x a) t_0 & 2i \sin(k_x a) t_1 & 2 \cos(k_x a) t_2 \\ -2i \sin(k_x a) t_1 & \epsilon_2 + 2 \cos(k_x a) t_{11} & 2i \sin(k_x a) t_{12} \\ 2 \cos(k_x a) t_2 & -2i \sin(k_x a) t_{12} & \epsilon_2 + 2 \cos(k_x a) t_{22} \end{bmatrix}, \quad (\text{A5})$$

$$h'_2 = \begin{bmatrix} 2 \cos(\frac{1}{2} k_x a) t_0 & i \sin(\frac{1}{2} k_x a) (t_1 - \sqrt{3} t_2) & -\frac{1}{2} \cos(\frac{1}{2} k_x a) (\sqrt{3} t_1 + t_2) \\ -i \sin(\frac{1}{2} k_x a) (t_1 + \sqrt{3} t_2) & \frac{1}{2} \cos(\frac{1}{2} k_x a) (t_{11} + 3 t_{22}) & -i \sin(\frac{1}{2} k_x a) (\frac{\sqrt{3}}{2} t_{11} + 2 t_{12} - \frac{\sqrt{3}}{2} t_{22}) \\ \cos(\frac{1}{2} k_x a) (\sqrt{3} t_1 - t_2) & -i \sin(\frac{1}{2} k_x a) (\frac{\sqrt{3}}{2} t_{11} - 2 t_{12} - \frac{\sqrt{3}}{2} t_{22}) & \frac{1}{2} \cos(\frac{1}{2} k_x a) (3 t_{11} + t_{22}) \end{bmatrix}. \quad (\text{A6})$$

The energy bands of a zigzag MoS₂ nanoribbon with $W = 8$ (using the GGA parameters in Table II) from both the TB model and FP calculations are given in Fig. 9. From the FP results, we know that the band 1 and 2 shown by arrows in Fig. 9 are the edge states from the d_{z^2} , d_{xy} , and $d_{x^2-y^2}$ orbitals of

Mo atoms at the two edges of the ribbon, band 3 is from the Mo- d_{yz} orbital at the Mo-terminated edge, and band 4 is from the S- p_y and p_z orbitals at the S-terminated edge. Due to the neglect of d_{xz} , d_{yz} and S- p orbitals in the TB model, band 3 and 4 do not exist in the TB bands. Nevertheless, band 1 and 2

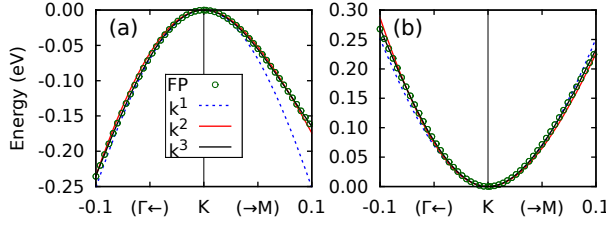


Figure 10: (color online) (a) Valence and (b) conduction bands in the K valley of monolayer MoS_2 , within the range of $0.1 \times \frac{2\pi}{a}$ in Γ and M directions. Open circles are FP results (GGA case). Blue dashed, red solid and black solid curves are the bands from the two-band $\mathbf{k} \cdot \mathbf{p}$ model of $H_{kp}^{(1)}$, $H_{kp}^{(2)}$ and $H_{kp}^{(3)}$ respectively. CBMs and VBMs are both shifted to 0. $a = 3.190 \text{ \AA}$ and $\Delta = 1.663 \text{ eV}$ for all. Other fitted parameters: $t = 1.105 \text{ eV}$ for $H_{kp}^{(1)}$; $t = 1.059 \text{ eV}$, $\gamma_1 = 0.055 \text{ eV}$, $\gamma_2 = 0.077 \text{ eV}$ and $\gamma_3 = -0.123 \text{ eV}$ for $H_{kp}^{(2)}$; $t = 1.003 \text{ eV}$, $\gamma_1 = 0.196 \text{ eV}$, $\gamma_2 = -0.065 \text{ eV}$, $\gamma_3 = -0.248 \text{ eV}$, $\gamma_4 = 0.163 \text{ eV}$, $\gamma_5 = -0.094 \text{ eV}$ and $\gamma_6 = -0.232 \text{ eV}$ for $H_{kp}^{(3)}$.

are given by the TB model reasonably. Therefore, the simple NN TB model for MX_2 zigzag ribbon can give satisfactory results, if the edge states band 1 and 2 are the focus of a study.

Appendix B: The two-band $\mathbf{k} \cdot \mathbf{p}$ model

It is clear from Fig. 3 that the three-band NN TB model is sufficient to describe the physics of conduction and valence bands in the K valley (also true for $-K$ valley due to the time reversal symmetry). Thus we can expand Eq. (4) in the $\pm K$ valleys to any order requested and then reduce it to a two-band $\mathbf{k} \cdot \mathbf{p}$ model in the Löwdin partitioning method.^{57,59,60} Using $|\psi_c^\tau\rangle = |d_{z^2}\rangle$ and $|\psi_v^\tau\rangle = \frac{1}{\sqrt{2}}(|d_{x^2-y^2}\rangle + i\tau|d_{xy}\rangle)$ ($\tau = \pm$ is the valley index) as bases, the obtained two-band $\mathbf{k} \cdot \mathbf{p}$ model up to the third order in \mathbf{k} (relative to τK) are

$$H_{kp}^{(1)}(\mathbf{k}; \tau) = \begin{bmatrix} \Delta/2 & at(\tau k_x - ik_y) \\ at(\tau k_x + ik_y) & -\Delta/2 \end{bmatrix}, \quad (\text{B1})$$

$$H_{kp}^{(2)}(\mathbf{k}; \tau) = H_{kp}^{(1)}(\mathbf{k}; \tau) + a^2 \begin{bmatrix} \gamma_1 k^2 & \gamma_3(\tau k_x + ik_y)^2 \\ \gamma_3(\tau k_x - ik_y)^2 & \gamma_2 k^2 \end{bmatrix}, \quad (\text{B2})$$

$$H_{kp}^{(3)}(\mathbf{k}; \tau) = H_{kp}^{(2)}(\mathbf{k}; \tau) + a^3 \begin{bmatrix} \gamma_4 \tau k_x (k_x^2 - 3k_y^2) & \gamma_6 k^2 (\tau k_x - ik_y) \\ \gamma_6 k^2 (\tau k_x + ik_y) & \gamma_5 \tau k_x (k_x^2 - 3k_y^2) \end{bmatrix}, \quad (\text{B3})$$

in which Δ is the bandgap at K , t and $\gamma_1 \sim \gamma_6$ are energy parameters, and $k^2 = k_x^2 + k_y^2$. Eq. (B1) is the massive Dirac Hamiltonian given in Ref. 18 which was derived just this way, and Eqs. (B2) and (B3) are consistent with previous works.^{29,31} In Fig. 10, the bands of monolayer MoS_2 from $H_{kp}^{(1)}$ capture the main physics in the valley but neglect the details such as the anisotropic dispersion (the trigonal warping) and the electron-hole asymmetry, the bands from $H_{kp}^{(2)}$ recover the aforementioned missing details, and the bands from $H_{kp}^{(3)}$ agree with the FP bands perfectly.

When SOC is considered to the first order, Eq. (27) is still valid and we can get

$$H_{kpso}^{(n)}(\mathbf{k}; \tau, s) = H_{kp}^{(n)}(\mathbf{k}; \tau) + \begin{bmatrix} 0 & 0 \\ 0 & \tau s \lambda \end{bmatrix}, \quad (\text{B4})$$

where $s = \pm 1$ is the spin index (+1 for \uparrow and -1 for \downarrow) since spin is a good quantum number. The $\tau s \lambda$ term in Eq. (B4) appears in the form of the product of the valley index τ , the spin index s , and the SOC parameter λ , which implies the rich physics due to the SOC induced coupling of valley and spin described in Ref. 18.

Appendix C: FP band structure calculations

The FP band structures used for fitting the parameters were calculated by the VASP package^{61,62} using the projector-augmented wave (PAW) method.^{63,64} Exchange-correlation functionals of both GGA⁶⁵ and LDA^{66,67} were used to give comparable results. The energy cutoff of plane wave basis was set to 400 eV and the convergence criterion 10^{-6} eV. A gamma-centered \mathbf{k} -mesh of $10 \times 10 \times 1$ was used and layer separation was greater than 15 \AA . For all monolayers of MX_2 , lattice constants were optimized and atomic positions were relaxed until the force on each atom was less than 0.005 eV/ \AA .

* wangyao@hku.hk

† dixiao@cmu.edu

¹ K. F. Mak, C. Lee, J. Hone, J. Shan, and T. F. Heinz, *Phys. Rev. Lett.* **105**, 136805 (2010).

² A. Splendiani, L. Sun, Y. Zhang, T. Li, J. Kim, C.-Y. Chim, G. Galli, and F. Wang, *Nano Lett.* **10**, 1271 (2010).

³ S. Tongay, J. Zhou, C. Ataca, K. Lo, T. S. Matthews, J. Li, J. C.

Grossman, and J. Wu, *Nano Lett.* **12**, 5576 (2012).

⁴ J. S. Ross, S. Wu, H. Yu, N. Ghimire, A. Jones, G. Aivazian, J. Yan, D. Mandrus, D. Xiao, W. Yao, and X. Xu, *Nature Commun.* **4**, 1474 (2013).

⁵ H. Zeng, G.-B. Liu, J. Dai, Y. Yan, B. Zhu, R. He, L. Xie, S. Xu, X. Chen, W. Yao, and X. Cui, *Scientific Reports* **3**, 1608 (2013).

⁶ B. Radisavljevic, A. Radenovic, J. Brivio, V. Giacometti, and

- A. Kis, *Nature Nanotech.* **6**, 147 (2011).
- ⁷ D. Lembke and A. Kis, *ACS Nano* **6**, 10070 (2012).
- ⁸ M.-W. Lin, L. Liu, Q. Lan, X. Tan, K. S. Dhindsa, P. Zeng, V. M. Naik, M. M.-C. Cheng, and Z. Zhou, *J. Phys. D* **45**, 345102 (2012).
- ⁹ W. Bao, X. Cai, D. Kim, K. Sridhara, and M. S. Fuhrer, *Appl. Phys. Lett.* **102**, 042104 (2013).
- ¹⁰ S. Larentis, B. Fallahzad, and E. Tutuc, *Appl. Phys. Lett.* **101**, 223104 (2012).
- ¹¹ H. Fang, S. Chuang, T. C. Chang, K. Takei, T. Takahashi, and A. Javey, *Nano Lett.* **12**, 3788 (2012).
- ¹² Q. H. Wang, K. Kalantar-Zadeh, A. Kis, J. N. Coleman, and M. S. Strano, *Nature Nanotech.* **7**, 699 (2012).
- ¹³ D. Xiao, W. Yao, and Q. Niu, *Phys. Rev. Lett.* **99**, 236809 (2007).
- ¹⁴ W. Yao, D. Xiao, and Q. Niu, *Phys. Rev. B* **77**, 235406 (2008).
- ¹⁵ O. Gunawan, Y. P. Shkolnikov, K. Vakili, T. Gokmen, E. P. De Poortere, and M. Shayegan, *Phys. Rev. Lett.* **97**, 186404 (2006).
- ¹⁶ A. Rycerz, J. Tworzydło, and C. W. J. Beenakker, *Nature Phys.* **3**, 172 (2007).
- ¹⁷ Z. Zhu, A. Collaudin, B. F. W. Kang, and K. Behnia, *Nature Phys.* **8**, 89 (2012).
- ¹⁸ D. Xiao, G.-B. Liu, W. Feng, X. Xu, and W. Yao, *Phys. Rev. Lett.* **108**, 196802 (2012).
- ¹⁹ T. Cao, G. Wang, W. Han, H. Ye, C. Zhu, J. Shi, Q. Niu, P. Tan, E. Wang, B. Liu, and J. Feng, *Nature Commun.* **3**, 887 (2012).
- ²⁰ K. F. Mak, K. He, J. Shan, and T. F. Heinz, *Nature Nanotech.* **7**, 494 (2012).
- ²¹ H. Zeng, J. Dai, W. Yao, D. Xiao, and X. Cui, *Nature Nanotech.* **7**, 490 (2012).
- ²² S. Wu, J. S. Ross, G.-B. Liu, G. Aivazian, A. Jones, Z. Fei, W. Zhu, D. Xiao, W. Yao, D. Cobden, and X. Xu, *Nature Phys.* **9**, 149 (2013).
- ²³ A. Jones, H. Yu, N. Ghimire, S. Wu, G. Aivazian, J. Ross, B. Zhao, J. Yan, D. Mandrus, D. Xiao, W. Yao, and X. Xu, (2013), 1303.5318.
- ²⁴ Z. Y. Zhu, Y. C. Cheng, and U. Schwingenschlögl, *Phys. Rev. B* **84**, 153402 (2011).
- ²⁵ X. Li, F. Zhang, and Q. Niu, *Phys. Rev. Lett.* **110**, 066803 (2013).
- ²⁶ H.-Z. Lu, W. Yao, D. Xiao, and S.-Q. Shen, *Phys. Rev. Lett.* **110**, 016806 (2013).
- ²⁷ F. Parhizgar, H. Rostami, and R. Asgari, *Phys. Rev. B* **87**, 125401 (2013).
- ²⁸ Z. Gong, G.-B. Liu, H. Yu, D. Xiao, X. Cui, X. Xu, and W. Yao, *Nature Commun.* **4**, 2053 (2013).
- ²⁹ H. Rostami, A. G. Moghaddam, and R. Asgari, (2013), 1302.5901.
- ³⁰ F. Zahid, L. Liu, Y. Zhu, J. Wang, and H. Guo, (2013), 1304.0074.
- ³¹ A. Kormányos, V. Zolyomi, N. D. Drummond, P. Rakytá, G. Burkard, and V. I. Fal'ko, (2013), 1304.4084.
- ³² E. Cappelluti, R. Roldán, J. A. Silva-Guillén, P. Ordejón, and F. Guinea, (2013), 1304.4831.
- ³³ T. Cheiwchanchamnangij and W. R. L. Lambrecht, *Phys. Rev. B* **85**, 205302 (2012).
- ³⁴ E. S. Kadantsev and P. Hawrylak, *Solid State Commun.* **152**, 909 (2012).
- ³⁵ H. Zeng, B. Zhu, K. Liu, J. Fan, X. Cui, and Q. M. Zhang, *Phys. Rev. B* **86**, 241301(R) (2012).
- ³⁶ K. Kośmider and J. Fernández-Rossier, *Phys. Rev. B* **87**, 075451 (2013).
- ³⁷ Y. Song and H. Dery, (2013), 1302.3627.
- ³⁸ R. A. Bromley, R. B. Murray, and A. D. Yoffe, *J. Phys. C* **5**, 759 (1972).
- ³⁹ L. F. Mattheiss, *Phys. Rev. B* **8**, 3719 (1973).
- ⁴⁰ S. Lebègue and O. Eriksson, *Phys. Rev. B* **79**, 115409 (2009).
- ⁴¹ C. Ataca, H. Şahin, and S. Ciraci, *J. Phys. Chem. C* **116**, 8983 (2012).
- ⁴² Y. Ding, Y. Wang, J. Ni, L. Shi, S. Shi, and W. Tang, *Physica B: Condensed Matter* **406**, 2254 (2011).
- ⁴³ C. Ataca and S. Ciraci, *J. Phys. Chem. C* **115**, 13303 (2011).
- ⁴⁴ S. Bhattacharyya and A. K. Singh, *Phys. Rev. B* **86**, 075454 (2012).
- ⁴⁵ J. Kang, S. Tongay, J. Zhou, J. Li, and J. Wu, *Appl. Phys. Lett.* **102**, 012111 (2013).
- ⁴⁶ P. Johari and V. B. Shenoy, *ACS Nano* **6**, 5449 (2012).
- ⁴⁷ H. Peelaers and C. G. Van de Walle, *Phys. Rev. B* **86**, 241401(R) (2012).
- ⁴⁸ W. S. Yun, S. W. Han, S. C. Hong, I. G. Kim, and J. D. Lee, *Phys. Rev. B* **85**, 033305 (2012).
- ⁴⁹ H. Shi, H. Pan, Y.-W. Zhang, and B. I. Yakobson, (2012), 1211.5653.
- ⁵⁰ S. Horzum, H. Sahin, S. Cahangirov, P. Cudazzo, A. Rubio, T. Serin, and F. M. Peeters, (2013), 1302.6635.
- ⁵¹ W. Feng, Y. Yao, W. Zhu, J. Zhou, W. Yao, and D. Xiao, *Phys. Rev. B* **86**, 165108 (2012).
- ⁵² Y. Yao, L. Kleinman, A. H. MacDonald, J. Sinova, T. Jungwirth, D.-S. Wang, E. Wang, and Q. Niu, *Phys. Rev. Lett.* **92**, 037204 (2004).
- ⁵³ D. Xiao, M.-C. Chang, and Q. Niu, *Rev. Mod. Phys.* **82**, 1959 (2010).
- ⁵⁴ Y. Yao and Z. Fang, *Phys. Rev. Lett.* **95**, 156601 (2005).
- ⁵⁵ H. Ochoa and R. Roldán, *Phys. Rev. B* **87**, 245421 (2013).
- ⁵⁶ For WSe₂ monolayer, the band with d_{+1} orbital above the bandgap is the 5th band above the bandgap, while it is the 4th band above the bandgap for other MX_2 monolayers.
- ⁵⁷ R. Winkler, *Spin-orbit Coupling Effects in Two-Dimensional Electron and Hole Systems*, Springer Tracts in Modern Physics, Vol. 191 (Springer, Berlin, 2003).
- ⁵⁸ D. Xiao, W. Zhu, Y. Ran, N. Nagaosa, and S. Okamoto, *Nature Commun.* **2**, 596 (2011).
- ⁵⁹ P.-O. Löwdin, *J. Chem. Phys.* **19**, 1396 (1951).
- ⁶⁰ J. M. Luttinger and W. Kohn, *Phys. Rev.* **97**, 869 (1955).
- ⁶¹ G. Kresse and J. Furthmüller, *Phys. Rev. B* **54**, 11169 (1996).
- ⁶² G. Kresse and J. Furthmüller, *Comput. Mater. Sci.* **6**, 15 (1996).
- ⁶³ P. E. Blöchl, *Phys. Rev. B* **50**, 17953 (1994).
- ⁶⁴ G. Kresse and D. Joubert, *Phys. Rev. B* **59**, 1758 (1999).
- ⁶⁵ J. P. Perdew, K. Burke, and M. Ernzerhof, *Phys. Rev. Lett.* **77**, 3865 (1996).
- ⁶⁶ D. M. Ceperley and B. J. Alder, *Phys. Rev. Lett.* **45**, 566 (1980).
- ⁶⁷ J. P. Perdew and A. Zunger, *Phys. Rev. B* **23**, 5048 (1981).